Nanostructure-based finite element analyses of aluminium profiles subjected to quasi-static axial crushing

Henrik Granum[a,*], Ole Runar Myhr[a,b,c], Tore Børvik[a,c], Odd Sture Hopperstad[a,c]
[a]*Structural Impact Laboratory (SIMLab), Norwegian University of Science and Technology, N-7491 Trondheim, Norway*
[b]*Hydro Aluminium, Research and Technology Development (RTD), NO-6601 Sunndalsøra, Norway*
[c]*Centre for Advanced Structural Analysis (CASA), NTNU, NO-7491 Trondheim, Norway*

Keywords: Aluminium alloys; nanoscale model; energy absorption; crashworthiness; finite element analysis

Abstract

In this study, a nanostructure model is used to predict the stress-strain curves of the aluminium alloys AA6063, AA6061 and AA6110 in T6, T7 and O tempers based on the chemical composition and the thermo-mechanical history. The predicted stress-strain curves are then employed in finite element analyses of rectangular hollow section (RHS) profiles of the same materials subjected to axial quasi-static crushing. Thus, the simulations are performed without any calibration of the plasticity model based on material tests. In addition, simulations with the material model calibrated from tensile tests on the same materials are performed for comparison. An experimental programme of the RHS profiles is conducted for validation purposes and compared to the numerical results in terms of the force-displacement curves and the peak and mean forces. To put emphasis on the performance of the nanostructure model, a refined solid element model is used to capture accurately the deformed geometry during axial crushing. A separate study is conducted to investigate the effect of friction on the simulated behaviour of the profiles. The numerical and experimental force-displacement curves display good agreement with deviations in the mean absolute percentage error (MAPE) of the peak and mean force less than 10 % and 8 %, respectively. By visual inspection of the deformed profiles, excellent agreement is found between the numerical simulations and the experimental tests. The results suggest that the nanostructure model can be used with confidence in design of energy absorbing structural components made of 6xxx aluminium alloys.

1 Introduction

Aluminium is favourable in a number of engineering applications due to its low weight-to-stiffness ratio. Among the many applications are automotive, offshore, protective and aerospace structures. Aluminium alloys have also entered into new application areas during the last several

*Corresponding author.
E-mail address: henrik.granum@ntnu.no (Henrik Granum)
URL: http://www.ntnu.edu/kt/fractal

decades due to the development of new alloys with improved properties, often replacing steel as the preferred material. From an environmental point of view, the recyclability of aluminium compared to steel makes it favourable as a future-oriented construction material. In the automotive industry, the introduction of aluminium components has contributed to lower the CO_2 emission and fuel consumption due to weight savings. Other advantageous properties of aluminium include high corrosion resistance, and high electrical and thermal conductivity. Aluminium alloys with specific properties are often required and the possibility to tailor an alloy to given properties would be beneficial.

In 6xxx alloys, the yield strength and the work hardening depend on the chemical composition and the thermo-mechanical history. Nanostructure models able to predict the flow stress from the chemical composition and the thermo-mechanical history of 6xxx alloys have been under development for the last few decades. By use of such models, flow stress curves can be obtained without carrying out any mechanical tests and thus enable simulation-based design of structures made of 6xxx alloys.

The nanostructure model NaMo, which was developed for 6xxx alloys by Myhr et al. [1], has been used with success in different applications on a variety of different alloys. Johnsen et al. [2] conducted ballistic impact experiments on the wrought AA6070 in four different temper conditions. The stress-strain behaviour was predicted by NaMo and used in non-linear finite element simulations with good correlation to the experimental tests. The ballistic limit velocity and the flow stress curves were reported with a maximum deviation of less than 10 % between the numerical and experimental results. Holmen et al. [3] conducted experiments on MIG-welded AA6082-T6 extrusions struck by small-arms bullets. A spatial distribution of the stress-strain behaviour at ambient temperature was determined by NaMo from the chemical composition, artificial ageing history and welding procedure. The resulting flow stress curves were functions of the distance from the weld centre line and used in a 3D finite element model to investigate the effect of the heat affected zone (HAZ) on the ballistic properties. The numerical simulations were found to be in good correspondence with the experimental results and the ballistic limit velocities were within 10 % of the experimental ones. In Hoang et al. [4], square hollow section AA6060 profiles subjected to quasi-static axial crushing were investigated. The profiles were artificially aged to three different tempers using two different cooling rates after solution heat treatment. The flow stress curves were predicted by NaMo, where the incubation time was included in the simulations by a new feature in the model, and good agreement between the experimental and numerical results was reported. Engler et al. [5] investigated the effect

of natural ageing and pre-straining on the strength and anisotropy of AA6016. Tensile tests with varying room temperature storage time and pre-straining were conducted to obtain stress-strain curves for the alloy-temper combinations. Corresponding stress-strain curves were calculated by NaMo and compared to the experimentally obtained ones. It was reported that the curves predicted by NaMo captured the main trends, even though they consistently underestimated the flow stress compared with the measured values.

Crashworthiness of aluminium profiles has been studied extensively in recent years, both experimentally and numerically. The strive to optimize the energy absorbing capability during car crashes has led to studies on a variety of geometries and materials. Zhang et al. [6] studied axial crushing of square multi-cell columns of AA6060-T4. It was found that by introducing internal webs to the columns, the energy absorption capability was improved when comparing plain columns of equal weight. An increased energy absorption efficiency of 50 % was reported by substituting a single-cell column with a 3 × 3 column of equal weight. In Zhang et al. [7], square AA6061-O tubes with graded thickness subjected to quasi-static axial loading were investigated experimentally and numerically. Two types of thickness distributions were tested and the results showed that introducing a thickness gradient to a tube might increase the energy absorption capability significantly and an increase in mean force of up to 35 % compared to non-graded tubes was reported. However, the problems of material fracture and mode switch were addressed as a potential effect of too excessive grading. The numerical simulations reflected the trends seen in the experiments, and the deviation was less than 16 %. Optimization of the tubes was performed by use of the response surface methodology (RSM) to obtain an optimal cross-section for a square tube. Results showed that increasing the wall-thickness in the corners increased the energy absorption capability. Sun et al. [8] studied the energy absorption capability of multi-corner profiles of AA6060 subjected to dynamic axial impact. It was shown numerically that increasing the number and size of corners in a profile had an effect on the energy absorption capability and that multi-corner profiles increased the crushing force efficiency with 12 % compared to square tubes of equal weight. Aluminium alloy profiles have also been studied extensively in combination with foam fillers and other reinforcements, see e.g. [9]–[15].

The main objective of this study is to investigate the accuracy of the nanostructure model NaMo for a range of alloy-temper combinations by employing the predicted stress-strain curves in nonlinear finite element (FE) simulations of RHS profiles subjected to quasi-static axial crushing. To evaluate the accuracy of the flow stress curves predicted by NaMo for application in design of energy absorbing structures, tensile tests and quasi-static axial crushing tests are performed for the same array of alloy-

temper combinations. Section 2 presents the alloys and heat treatments, the tensile tests and the axial crushing tests, whereas Section 3 gives an overview of the nanostructure model NaMo and presents the calculated flow stress curves for all combinations of alloy and heat treatment. In Section 4, the FE model of the axial crushing test and the numerical results, obtained with the IMPETUS Afea Solver [16], are presented. The numerical results are discussed in Section 5, and the main observations and conclusions are summarized in Section 6.

2 Experimental study

2.1 Alloys and heat treatments

Three different 6xxx aluminium alloys are investigated in this study: AA6063, AA6061 and AA6110. The alloys were provided by Hydro Aluminium and received as billets with 95 mm diameter and 200 mm length. The chemical composition of the alloys is given in Table 1. The casting length was roughly 1.5 m and the casting conditions were according to standard guidelines for the designated alloys. Prior to extrusion, the ingots were homogenized at 575°C with a heating rate of 200°C per hour from room temperature and held for 2 h 15 min before cooling to room temperature at 400°C per hour. The profiles were extruded as RHS profiles with a wall thickness of 2.8 mm and a cross-section of 37 mm × 29 mm (see Figure 1), corresponding to a reduction ratio of about 19. The billets were pre-heated to 500°C before extrusion and the extruded profiles were water-quenched about 0.5 meters from the outlet of the die. Approximately the first half meter of the extruded profile for each new alloy was discarded due to possible contaminants in the press. After a short ramp-up time, the ram speed was held constant at 12.1 mm/s for AA6063 and 6.1 mm/s for AA6061 and AA6110. Afterwards, the profiles were cut into lengths of 175 cm and cold-deformed 0.5 % by stretching between 1 and 4 h after extrusion. The profiles were then stored at room temperature for 48 h followed by artificial ageing at 185°C for 8 h to obtain the peak strength temper T6. Selected profiles were further artificially aged to obtain the over-aged temper T7 and the soft annealed temper O, by holding at 185°C for another 168 h and at 410°C for 4 h, respectively. Having full control of the chemical composition and the details in the thermo-mechanical history of the material is important for the predictions of the nanostructure model NaMo presented in Section 3.

Table 1: Chemical composition of the different alloys in wt-%.

	Si	Mg	Fe	Mn	Ti	Zn	Cu	Cr	Al
AA6063	0.512	0.470	0.206	0.047	0.006	0.003	0.001	0.001	Balance
AA6061	0.621	0.903	0.209	0.038	0.106	0.054	0.204	0.060	Balance
AA6110	0.720	0.828	0.196	0.506	0.026	0.003	0.203	0.157	Balance

The profiles were cut into lengths of 100 mm with a geometrical trigger on the two long sides, as shown in Figure 1, using wire erosion to ensure good repeatability and symmetric progressive folding. This type of geometrical trigger was used with success in Ref. [17] and was accordingly adopted for this study. Prior to testing, the wall thickness of the profiles was measured at various positions and the profiles were weighed.

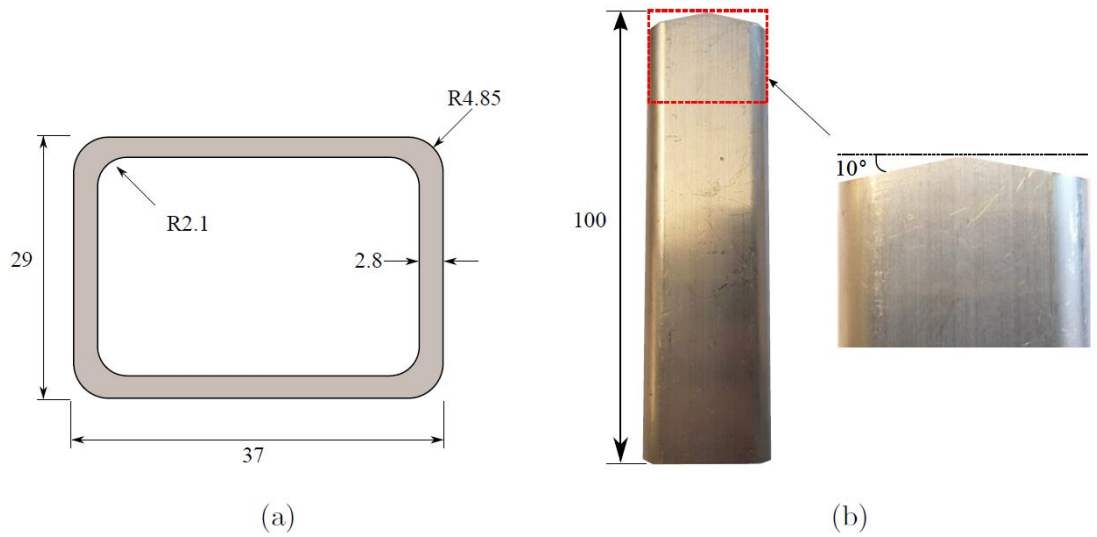

Figure 1: (a) Nominal cross-sectional geometry of profile and (b) visualization of the geometrical trigger used in the tests. Measures not specified are in mm.

2.2 Tensile tests

Uniaxial tensile tests were conducted for all nine alloy-temper combinations, using specimens taken from each of the four walls of the profiles along the extrusion direction. The dog-bone specimens had a gauge length of 20 mm and an initial thickness of 2.8 mm, i.e., similar to the wall thickness of the profile. The tensile tests were conducted in an Instron 5985 series universal testing machine at ambient temperature with a 5 kN load cell at an initial strain rate of 5×10^{-4} s^{-1}. The force was continuously measured by the load cell and the displacement of the gauge section was

tracked using digital image correlation (DIC) by a virtual extensometer. To enable the specimen for DIC, a speckle pattern was spray-painted on the gauge section and a Prosilica GC2450 camera oriented perpendicular to the gauge surface captured pictures at a resolution of 2448×802 pixels. The pictures from the camera and the measurements from the load cell were synchronized, operating at 2 fps. The spread among three corresponding tests was insignificant and the test experiencing median force level within an alloy-temper combination was chosen as representative test for calibration of the flow stress curves. The representative engineering stress-strain curves for all alloy-temper combinations are displayed in Figure 2. The large variation in strength and work hardening capacity between the different alloy-temper combinations is evident with yield strengths ranging from around 50 MPa to more than 300 MPa and tensile strengths between 100 MPa and 350 MPa.

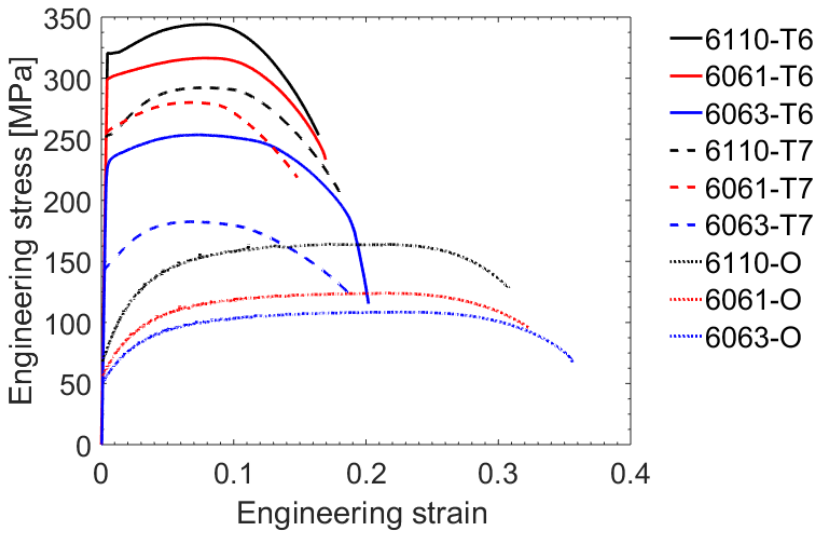

Figure 2: Engineering stress-strain curves for the nine alloy-temper combinations from tensile tests.

An FE model of the tensile specimen was made in Abaqus/Standard with 8-node trilinear brick elements with reduced integration. The model had six elements over the thickness, which gave an element size just below 0.5 mm. The material behaviour was represented by a rate-insensitive J_2-plasticity model, including the von Mises yield criterion, the associated flow rule and isotropic hardening. The flow stress σ_f was defined by

$$\sigma_f(\varepsilon_p) = \sigma_0 + \sum_{i=1}^{2} Q_i \left(1 - \exp\left(-C_i \varepsilon_p\right)\right) \quad (1)$$

where σ_0 is the initial yield stress, Q_i and C_i are parameters in the two-term Voce hardening rule, and ε_p is the equivalent plastic strain. As the aim of this study is to predict the overall behaviour of the profiles during axial crushing, represented by the peak force, energy absorption and folding pattern,

it was found appropriate to neglect the plastic anisotropy of the extruded profiles and to use the von Mises yield function. However, in studies of formability, plastic forming or ductile fracture of extruded aluminium profiles, the high-exponent Hershey yield function [18] is deemed more appropriate for materials with random texture and a high-exponent, linear transformation-based anisotropic yield criterion, like the Yld2004-18p criterion proposed by Barlat and co-workers [19], for textured materials.

The optimization tool LS-OPT was used to calibrate the hardening parameters (Q_i, C_i) by running sequential simulations on the same model with different input data. The engineering stress-strain curves from the representative tests shown in Figure 2 were calculated for each alloy-temper combination by use of a 16 mm virtual extensometer in the DIC software. This provides us with engineering stress-strain curves valid until failure, which were used as target curves in the optimization. An initial calibration of the hardening parameters up to necking was done in a spreadsheet and used as starting values for the optimization. A genetic algorithm was applied for the optimization and 100 equidistant regression points were used to ensure good fit in all parts of the curve. The optimal values of the hardening parameters were found by minimizing the mean square error between the simulated and experimental curves all the way to failure. The obtained parameters are given in Table 2, whereas the flow stress curves to 20 % plastic strain are depicted in Figure 3. It is seen that AA6110 has the highest strength for all tempers closely followed by AA6061, whereas AA6063 has the lowest strength of the three alloys. For a given alloy, temper O exhibits the lowest yield strength and highest work hardening, whereas temper T6 exhibits the highest yield strength and lowest work hardening. Temper T7 falls in-between the peak aged T6 condition and the soft annealed O condition.

Table 2: Parameters of the two-term Voce rule for the calibrated flow stress curves from tests.

Alloy	Temper	σ_0 (MPa)	Q_1 (MPa)	C_1	Q_2 (MPa)	C_2
AA6063	T6	233.0	40.0	19.9	34.7	5.0
	T7	142.0	46.0	39.4	24.0	9.1
	O	50.2	46.7	38.2	81.9	2.8
AA6061	T6	298.2	51.1	13.6	18.4	13.1
	T7	254.5	40.1	19.1	19.7	28.6
	O	56.3	47.9	42.1	80.2	4.4
AA6110	T6	320.4	43.3	18.7	30.6	12.7
	T7	251.3	64.5	19.4	19.2	22.1
	O	68.0	92.6	32.8	144.9	1.6

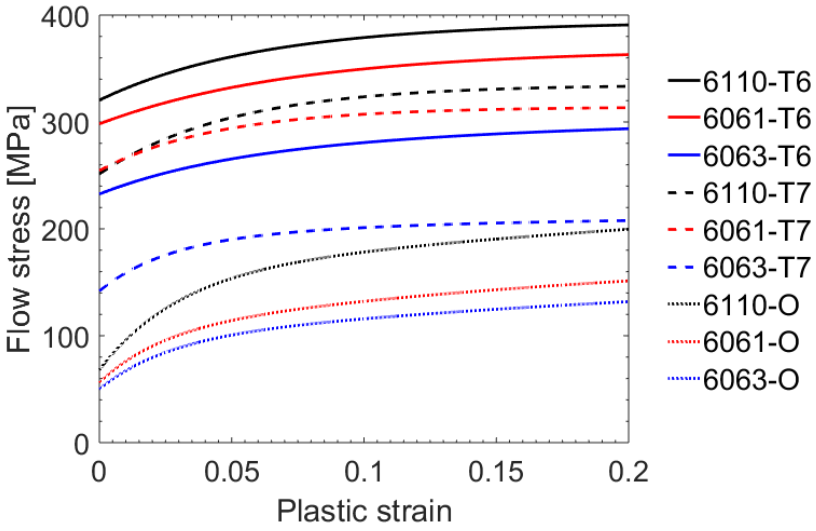

Figure 3: Flow stress curves to 20 % plastic strain for the nine alloy-temper combinations based on tensile tests and optimization using FE analysis.

2.3 Axial crushing tests

The crushing experiments were performed in an Instron 5985 series 250 kN testing machine at ambient temperature. The velocity of the cross-head was set to 30 mm/min and the profiles were deformed 67 mm. Two Prosilica GC2450 cameras operating at 5 fps with a resolution of 2448×1600 pixels captured the deformation from different angles. The axial force and displacement histories were recorded during the experiments. The profiles were placed directly on the level steel platen below the load cell, and no effort was put into constraining the boundary. The three alloys were all tested in the

three temper conditions obtained, resulting in nine different alloy-temper combinations. The test for each alloy-temper combinations was repeated two times, resulting in a total of 27 tests.

The force-displacement curves from the experiments are given in Figure 4, and the progress of an AA6063-T7 test is shown in Figure 5. From the force-displacement curves it is seen that the repeatability for the different alloy-temper combinations is excellent due to the geometrical trigger shown in Figure 1b. Some minor discrepancies are found between some repetitions at certain displacements, but the overall repeatability is deemed excellent. The scatter between repeated tests was less than 3 % in peak force and less than 2 % in mean force. The force-displacement curves for AA6110-T7 and AA6061-T7 seem to coincide, while the differences in the T6 temper are seen to be small between these two alloys. However, a notable difference is obtained in the O temper condition, where AA6110 is considerably higher in strength than AA6061. In general, the AA6063 alloy has notably lower strength than the other alloys for the different temper conditions, but the overall behaviour is similar as the force-displacement curves are shifted compared to the other alloys. All tests for T6 and T7 temper give four peaks in the force-displacement curves, while the tests for O temper give three fully developed peaks. As seen in Figure 5, the folding pattern for the AA6063-T7 experiment is symmetric and progressive. The first fold is initiated near the top of the profile confirming that the geometrical trigger works as desired, and the number of folds is coinciding with the number of peaks in the force-displacement curves. By visual inspection of the folded profiles, minor cracks were found in some corners for AA6061-T6 and AA6110-T6, while the other seven alloy-temper combinations have no indication of cracks. This is consistent with the presumption that the T6 temper is less ductile than the T7 and O tempers, and that higher strength comes at the cost of lower ductility.

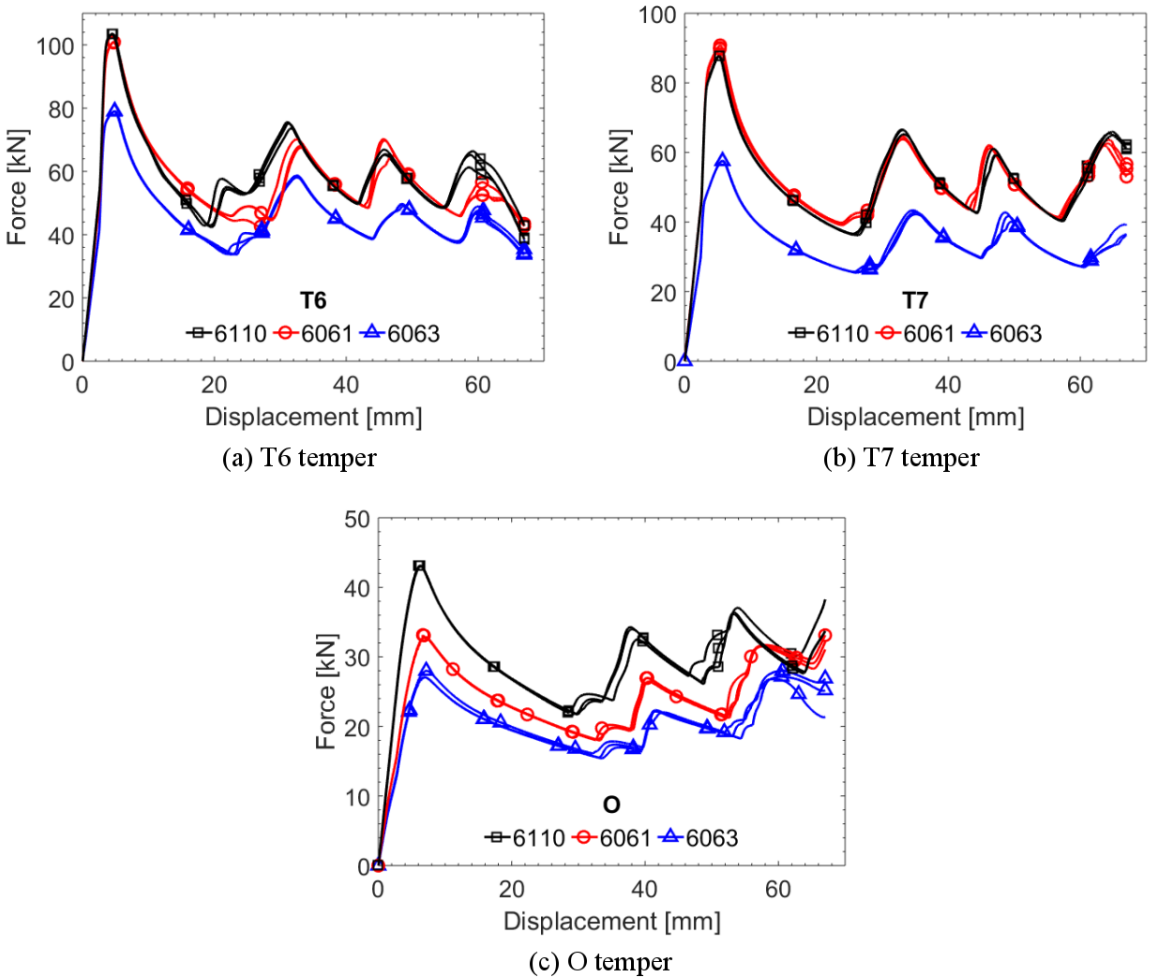

Figure 4: Force-displacement curves from the axial crushing tests for the different alloy-temper combinations.

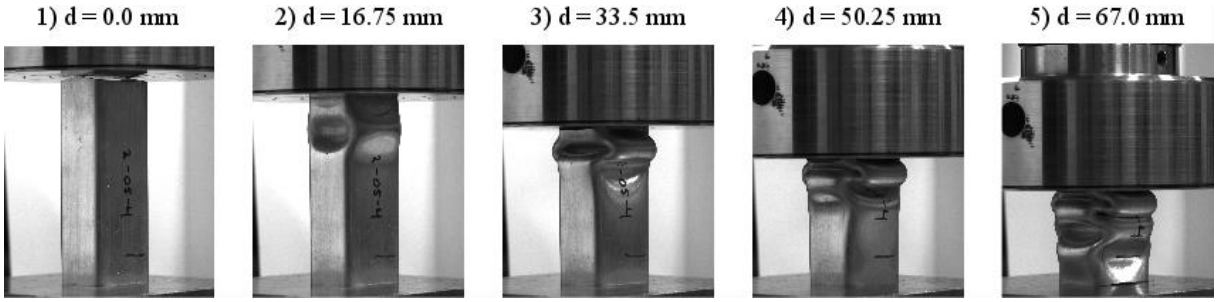

Figure 5: Deformation patterns from a test on an AA6063-T7 profile.

3 Nanostructure model (NaMo)

The nanostructure model NaMo [1][20] is a nanoscale material model composed of three interacting sub-models: a precipitation model, a yield strength model and a work hardening model. NaMo is developed for all 6xxx alloys and the present version is thoroughly validated against

experimental data from hot- and cold-rolled AA6005 plates as well as extrusions of AA6060 and AA6005. The model is calibrated once against these experimental data, and no further calibration is needed between simulations. The software is integrated in a computer code with a graphical user interface. Figure 6 describes the course of the program and the contributions from the different sub-models. The input to the model is the chemical composition of the alloy and the thermo-mechanical history, which are employed in the precipitation model. The output from the precipitation model is then given as input to the yield strength model and the work hardening model, which combined give the complete flow stress curve at room temperature, assuming isotropic material behaviour. The version used in this paper is an extended version, including the combined effect of cold deformation and prolonged room temperature storage on the subsequent response of artificial ageing, referred to as NaMo version 2 [20].

In the precipitation model, the evolution of the hardening precipitates by nucleation, growth or dissolution and coarsening is computed. There are three governing components in the precipitation model: 1) a nucleation law that predicts the number of stable nuclei forming at each time step, 2) a rate law that calculates the dissolution or growth rate of each discrete particle size class, and 3) a continuity equation that keeps track of the amount of solute being tied up in precipitates. In the present model, two different particle size distributions (PSDs) are calculated to represent different types of precipitates and clusters that tend to form in different temperature regions during thermo-mechanical processing, as determined by the individual nucleation laws that are associated with each PSD.

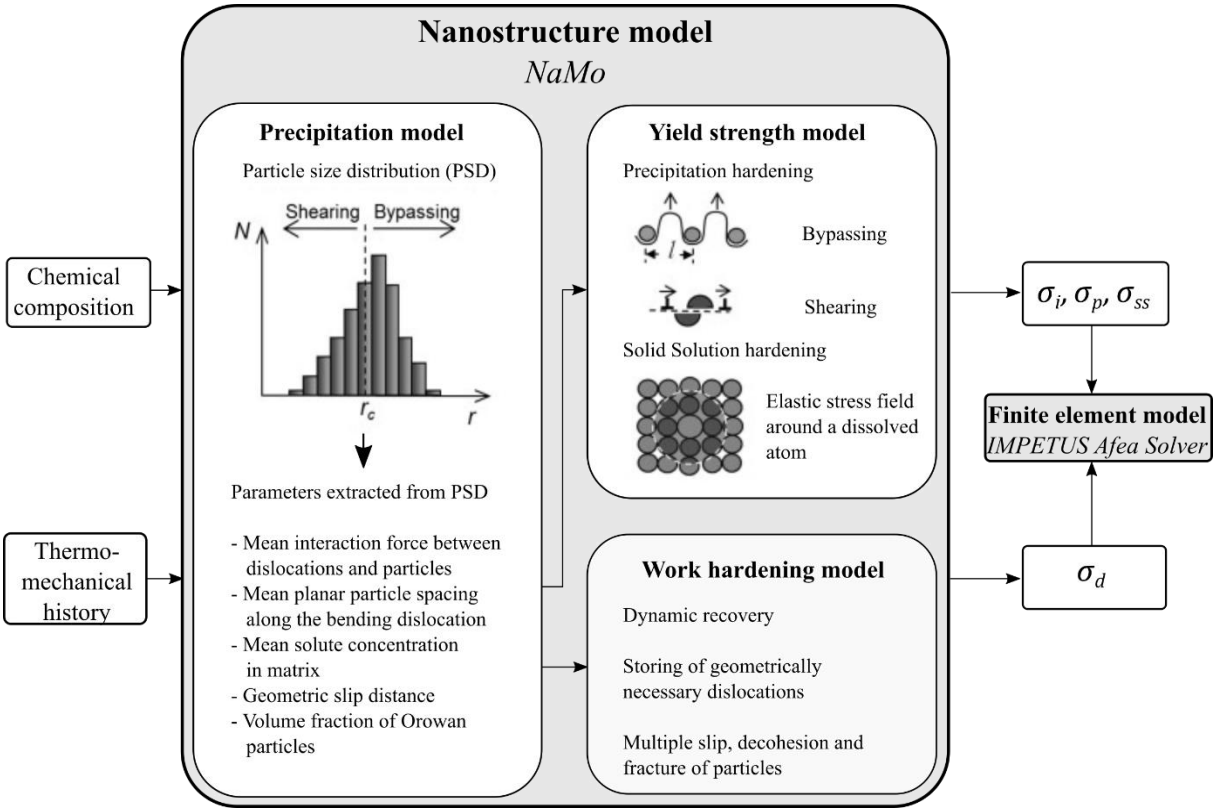

Figure 6: Outline of NaMo [3].

The first PSD is for β'' and β' particles which are nucleated during artificial ageing, while the second is for clusters which form during natural ageing. The two PSDs are linked together by the continuity equation. This leads to a complex balance between the two PSDs since the particles in each distribution consume solute as they grow. The consequence is that one PSD tends to evolve on the expense of the other at a given temperature. This is typically the case when clusters formed by natural ageing dissolve during the subsequent artificial ageing heat treatment, as hardening β'' and β' particles form. An example of this is shown in Figure 7a for AA6061 after the T6 ageing heat treatment. At this stage of the ageing, the two PSDs co-exist, even though the one for clusters is about to disappear completely since the clusters are too small to be stable at an ageing temperature of 185°C. Hence, after the T6 heat treatment, the predicted number density of clusters is only ~10^{18} #/m^3, compared with ~10^{22} #/m^3 for β'' and β' particles. Prolonged ageing corresponding to the overaged (T7) condition, or ageing at a higher temperature to give the O temper leads to complete dissolution of the clusters formed at room temperature, and only the PSD for β'' and β' particles survives. A comparison of this PSD for the three temper conditions T6, T7 and O is shown in Figure 7b. From the figure, it is evident that the mean radius increases and the overall number density decreases when going from the T6 to the T7 and eventually to the O condition. The mean particle radius for the two extreme conditions, i.e., T6 and O, is 5.2 nm and 126 nm, respectively. Plots of the resulting PSDs for

the remaining alloys, i.e., AA6063 and AA6110, show qualitatively similar trends as the ones for AA6061 in Figure 7, and are therefore not presented here for brevity.

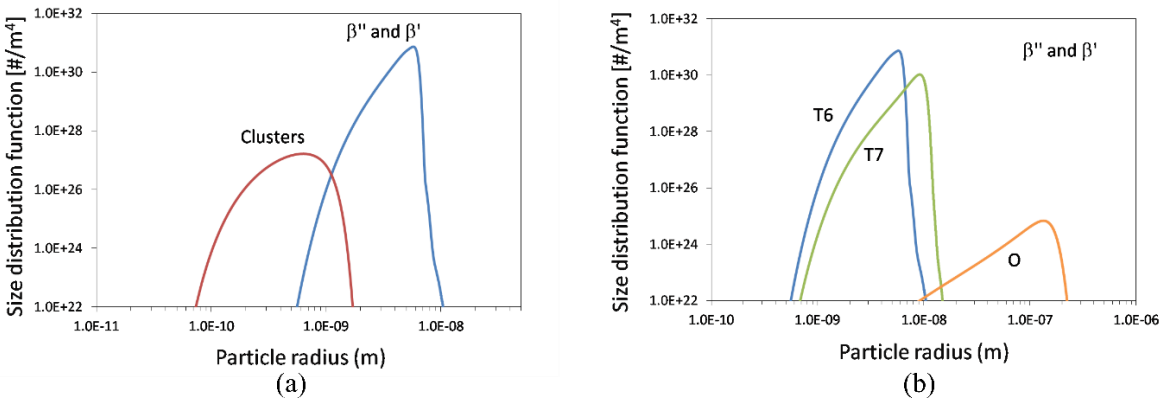

Figure 7: Predicted PSDs from NaMo for AA6061 showing (a) two co-existing PSDs for clusters and β'' and β' after T6 ageing, and (b) comparison of the PSD for β'' and β' for tempers T6, T7 and O.

The predicted PSDs in Figure 7 are input to the yield strength and work hardening models, as illustrated in Figure 6. In this figure, the columns in the PSD correspond to a certain number density within a specific particle radius class. Beyond a critical particle radius, the particles are assumed non-shearable by dislocations. This is obviously unreasonable for clusters from a physically point of view, since they are fully coherent with the aluminium matrix and cannot be bypassed by the dislocations. The critical particle radius will in this case be hypothetical and is only used as a scaling parameter in the yield strength model as explained in Ref. [20]. The PSDs change continuously during natural and artificial ageing, and the associated parameters are extracted and transferred to the yield strength and work hardening model at each time step of the simulation, as illustrated in Figure 6.

In the yield strength model, the overall macroscopic flow stress is given as

$$\sigma_f(\varepsilon_p) = \sigma_i + \sigma_p + \sigma_{ss} + \sigma_d(\varepsilon_p) \tag{2}$$

where σ_i corresponds to the intrinsic yield strength of pure aluminium, σ_p is the overall precipitation hardening contribution, σ_{ss} is the contribution from alloying elements in solid solution, and σ_d is the contribution from dislocation hardening as a function of the plastic strain. The precipitation hardening contribution σ_p is calculated using the following relationship:

$$\sigma_p = \frac{M\bar{F}}{bl} \tag{3}$$

where M is the Taylor factor, b is the magnitude of the Burgers vector, $\bar{F}$ is the mean obstacle strength, and l is the effective particle spacing in the slip plane along the bending dislocation. Both $\bar{F}$ and l are

explicitly defined by the PSD as explained in Ref [20]. Eq. (3) therefore represents a direct coupling between the precipitation model and the yield strength model. The overall strength contribution from particles, σ_p, contains the contributions from the two particle size distributions described above. These two strength contributions are denoted σ_{p1} and σ_{p2}, where the former represents clusters, and the latter metastable β'' and β' particles. σ_p is given by the following expression:

$$\sigma_p = \sqrt{\sigma_{p1}^2 + \sigma_{p2}^2} \tag{4}$$

In this equation, σ_{p1} and σ_{p2} are both calculated from Eq. (3) using individual values for $\bar{F}$ and l representing each of the two particle size distributions. The contribution from elements in solid solution to the flow stress, i.e., σ_{ss} in Eq. (2), is calculated as follows:

$$\sigma_{ss} = \sum_i k_i \, C_i^{2/3} \tag{5}$$

Here, C_i is the concentration of a specific element in solid solution and k_i is the corresponding scaling factor for the relevant elements with values given in Ref. [20]. For the elements Mg and Si, the solid solution concentrations, i.e., C_{Mg} and C_{Si}, vary during a heat treatment depending on the volume fraction of clusters and metastable particles.

The final term in Eq. (2), σ_d , represents the contribution from dislocations to the flow stress as calculated by the work hardening model. Two types of dislocations are considered: the statistically stored dislocations that are assumed to form anywhere in the material, and the geometrically necessary dislocations that are assumed to form close to large, non-shearable particles. The corresponding dislocation densities are denoted ρ_s and ρ_g, respectively, and the total dislocation density ρ is assumed to be the sum of the two. The resulting contribution from the dislocations to the flow stress, σ_d, is given by the following equation:

$$\sigma_d = \alpha M \mu b \sqrt{\rho_s + \rho_g} \tag{6}$$

where α is a constant with a value close to 0.3, and μ is the shear modulus.

For the statistically stored dislocations, the Kocks-Mecking relationship is used

$$\frac{\mathrm{d}\rho_s}{\mathrm{d}\varepsilon_p} = k_1 \sqrt{\rho_s} - k_2 \rho_s \tag{7}$$

Here, k_1 is a constant being characteristic for the material under consideration, whereas the parameter k_2 determines the rate of the dynamic recovery during plastic deformation. The parameter k_2 depends on the solute content of the alloy according to the following relation:

$$k_2 = k_1 \frac{\alpha M \mu b}{k_3 (C_{ss})^{\frac{3}{4}}} \tag{8}$$

In this equation, k_3 is a parameter which expresses the influence of solutes on k_2, and C_{ss} is an effective solid solution concentration, which includes a weighted overall effect of Mg and Si in solid solution on the dynamic recovery rate based on experiments.

The work hardening model predicts the evolution of dislocation densities ρ_s and ρ_g by evolution laws. A somewhat crude approximation in NaMo is that all particles are assumed to be spherical. Hardening precipitates like β'' and β' are either needle- or rod-shaped in Al-Mg-Si alloys. However, due to the initial calibration of the model, it can be argued that the assumption is reasonable based on the mathematical treatment provided in Ref. [20]. For geometrically necessary dislocations, the resulting dislocation density ρ_g depends on the magnitude of the geometric slip distance λ_g, which is a measure of how far the dislocations move before they are stored around the non-shearable particles that are dispersed within the material [21]. Thus, λ_g is a characteristic of the microstructure related to the type and distribution of the hardening precipitates in the material, and can be extracted from a given particle size distribution by the following expression:

$$\lambda_g = \left(8 \sum_{r=r_c}^{r=\infty} r_i^2 N_i \right)^{-1} \tag{9}$$

Here, N_i is the number of particles per unit volume within the size class r_i of the particle size distribution, and r_c is the critical radius above which the particles are bypassed by the dislocations and not sheared. Since only particles larger than r_c are capable of storing geometrically necessary dislocations, the work hardening model requires that the volume fraction of these particles f_o is estimated from the PSD containing the metastable $\beta''$and β' particles as follows:

$$f_o = \sum_{r=r_c}^{r=\infty} \frac{4}{3} \pi r_i^3 N_i \tag{10}$$

When λ_g and f_o are known from Eqns. (9) and (10) above, ρ_g can be predicted as described in Ref. [1]. The net contribution from dislocation hardening σ_d is calculated from a response equation as a function of the equivalent plastic strain ε_p as follows:

$$\sigma_d(\varepsilon_p) = \alpha M \mu b \sqrt{\left(\frac{k_1}{k_2}\right)^2 \left(1 - \exp\left(-\frac{k_2 \varepsilon_p}{2}\right)\right)^2 + \rho_{g,s}^{\mathrm{ref}} \frac{\lambda_g^{\mathrm{ref}}}{\lambda_g} \frac{\min(\varepsilon_p, \varepsilon_c)}{\varepsilon_c^{\mathrm{ref}}}} \qquad (11)$$

Here, index ref means a chosen reference alloy, and λ_g and λ_g^{ref} are geometric slip distances as defined in Eq. (9). The parameters ε_c and $\varepsilon_c^{\mathrm{ref}}$ are critical values of the equivalent plastic strain defining the saturation values for storing of geometrically necessary dislocations, which corresponds to a dislocation density $\rho_{g,s}^{\mathrm{ref}}$ for the reference alloy. The reader is referred to Refs. [1] and [20] for further details.

The flow stress curves of the different alloy-temper combinations predicted by NaMo were used to fit the parameters σ_0, Q_i and C_i of the work hardening rule in Eq. (1). The resulting hardening parameters are compiled in Table 3. It was found sufficient to use only one term in the Voce hardening rule for all but one alloy-temper combination for the NaMo curves, while in the calibration based on the tensile tests, two terms were needed to obtain adequate fits for all alloy-temper combinations. The flow stress curves from NaMo and the fitted curves (using the parameters in Table 3) are presented in Figure 8. The somewhat abrupt saturation point seen in the NaMo curves for the T6 and T7 tempers in Figure 8 is caused by the saturation of the density of geometrically necessary dislocations, cf. Eq. (11). However, the smoothly fitted curves are used in the subsequent FE simulations and the slope discontinuity is thus avoided.

Table 3: Parameters of the two-term Voce hardening rule for the NaMo-based flow stress curves.

Alloy	Temper	σ_0 (MPa)	Q_1 (MPa)	C_1	Q_2 (MPa)	C_2
AA6063	T6	232.5	4.5	298.0	57.8	21.0
	T7	138.6	49.0	35.4	-	-
	O	49.8	73.7	17.8	-	-
AA6061	T6	280.8	60.7	30.3	-	-
	T7	205.7	48.9	43.2	-	-
	O	70.5	73.7	18.0	-	-
AA6110	T6	312.2	60.8	30.9	-	-
	T7	234.6	48.8	44.8	-	-
	O	96.0	73.7	18.0	-	-

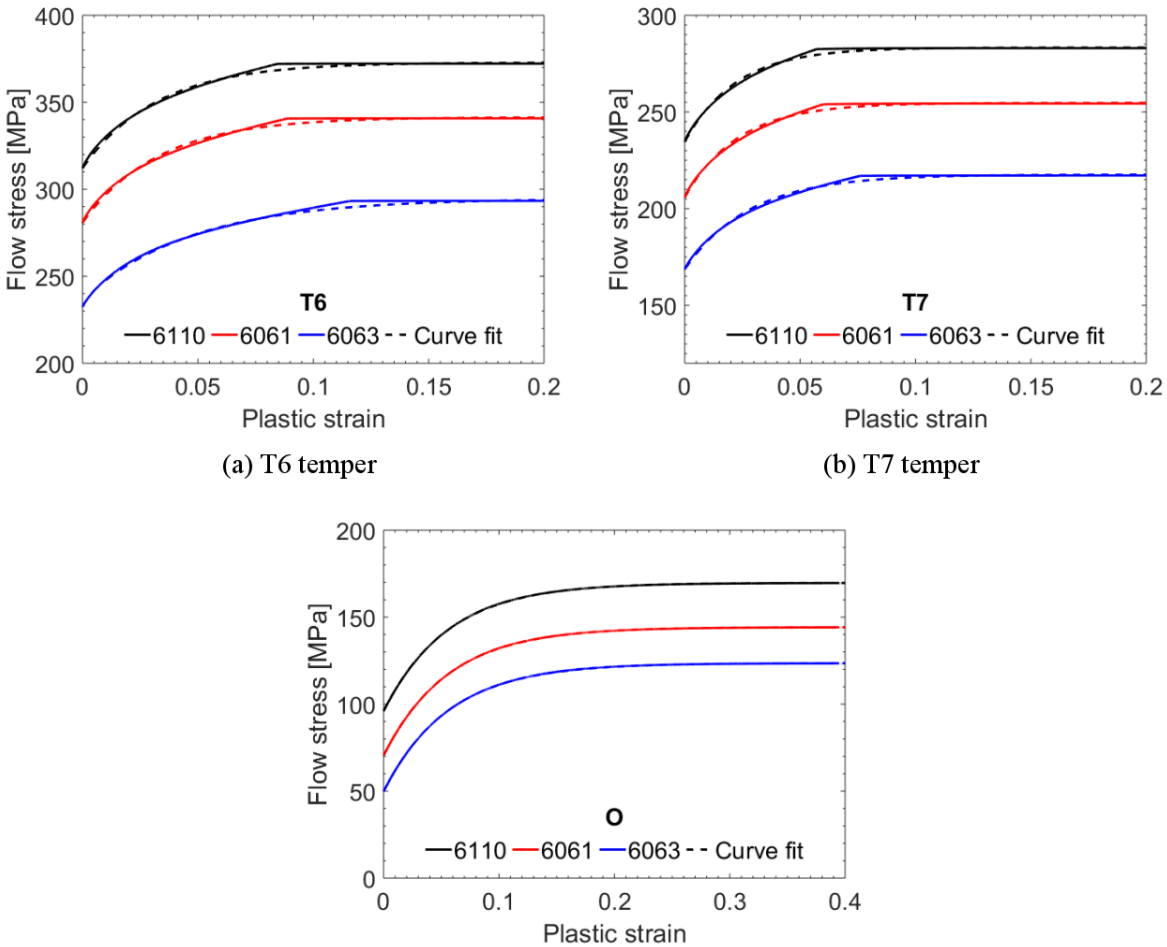

(a) T6 temper

(b) T7 temper

(c) O temper

Figure 8: Flow stress curves from NaMo simulations and fitted curves used in the FE analyses for the three alloys in temper (a) T6, (b) T7 and (c) O.

To obtain a quantitative comparison of the flow stress curves obtained based on the tensile tests and the NaMo calculations, scatter plots depicting the flow stress at 0.2 % plastic strain (i.e., the 0.2 % proof stress) and the flow stress at 20 % plastic strain are presented in Figure 9. The first plot, Figure 9a, illustrates the accuracy of the yield stress predicted with NaMo, whereas the second plot, Figure 9b, gives a measure of how well the work hardening is predicted. The scatter plots show that NaMo gives faithful predictions of the yield stress, even if the yield stress for AA6061-T7 is considerably underestimated. The predictions of the flow stress at 20 % plastic strain is slightly more accurate even though NaMo tends to underestimate the work hardening for a majority of the alloy-temper combinations. The mean absolute percentage error (MAPE) in the predicted yield stress and flow stress at 20 % plastic strain is 12 % and 9 %, respectively, which is deemed satisfactory as the predictions are made only based on chemical composition and heat treatment.

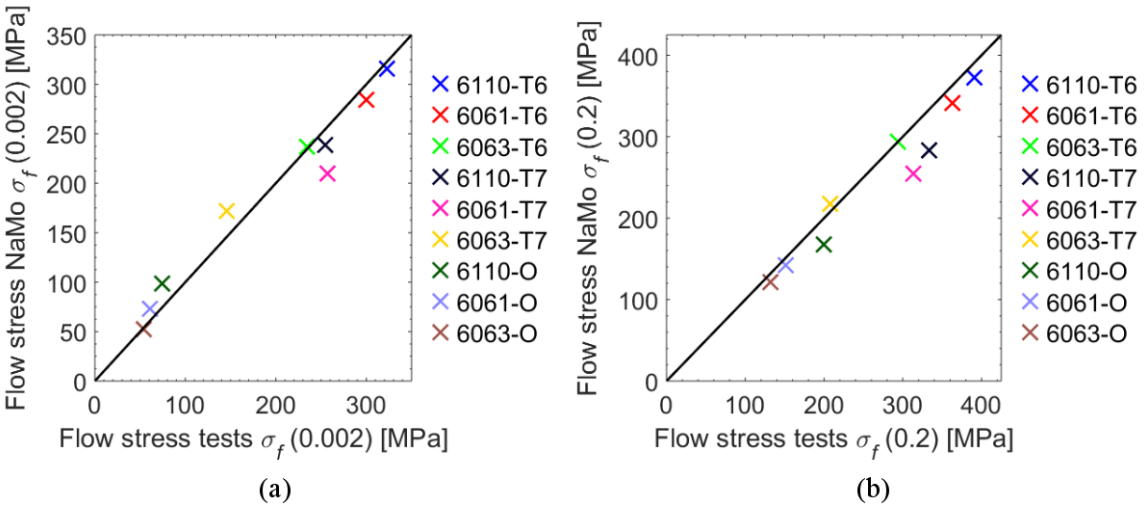

Figure 9: Scatter plots of (a) flow stress at 0.2 % plastic strain, i.e., $\sigma_f(0.002)$, and (b) flow stress at 20 % plastic strain, i.e., $\sigma_f(0.2)$, based on tensile tests and NaMo simulations.

4 Numerical simulations

4.1 Finite element model

The explicit FE code IMPETUS Afea Solver [16] was used to simulate the quasi-static axial crushing of the RHS profiles. The material behaviour was represented by a rate-insensitive J_2-plasticity model, including the von Mises yield criterion, the associated flow rule and isotropic hardening. The flow stress curve is defined by Eq. (1) with parameters given either in Table 2 or Table 3. The remaining material parameters are taken as nominal values for aluminium from the literature: Young's modulus, $E = 70000$ MPa, Poisson's ratio, $\nu = 0.3$, and density, $\rho = 2700$ kg/m^3.

The FE model consists of three parts: a rigid bottom plate, a rigid top plate and the profile, as shown in Figure 10a. By utilizing the symmetry of the problem, only a quarter of the profile was modelled according to the geometry presented in Figure 1. Assuming symmetric folding, this is a viable approach saving computational time and is employed in similar studies, see e.g. [4][7][11][12]. In previous numerical studies on axial crushing of profiles, see e.g. [4][7], three linear solid elements through the wall thickness were found to be sufficient. In this study, three fully integrated cubic 64-node hexahedron elements with third-order shape functions were employed through the wall thickness, known to be excellent in highly non-linear problems [16]. This gives an effective node spacing of approximately 0.3 mm, resulting in 10 nodes over the wall thickness. The through-thickness mesh is shown in Figure 10b. A thorough description of the applied higher order elements can be found in Holmen et al. [22]. A total of 11 118 elements and 348 244 nodes were employed in the quarter model. By employing a high-resolution mesh, the intention is to create an FE model that is sufficiently accurate to minimize the discretization errors and thus enable validation of the NaMo simulations. Prior to testing, the profiles were weighed and measured, allowing us to model the profile with the actual geometry obtained after the profiles were stretched 0.5 %. This resulted in an average wall thickness of 2.75 mm and an average weight of 83.8 g. The mass of the profile in the FE model was 83.9 g.

A gap of 0.1 mm was introduced between both the bottom and top plate and the profile to ensure no initial contact between the parts. The bottom plate was fixed against displacement and rotations, while the top plate was given a prescribed displacement of 67.2 mm towards the profile, resulting in axial loading. Both the bottom and top plates were modelled as rigid parts, requiring only the density as material input, which for steel was set to $\rho = 7850$ kg/m^3. The displacement was smoothly ramped up by a built-in feature in the FE code to a maximum velocity of 4.4 m/s to avoid inertia effects, and the energy balance was carefully checked to make sure that the kinetic energy was considerably lower than the internal energy, below 1 % in all simulations. Contact was taken care of by a penalty based node-to-surface algorithm, where Coulomb friction was specified in the contact. Both contact between the plates and the profile and self-contact of the profile walls were taken into consideration. Based on earlier studies on aluminium profiles subjected to axial loading, e.g. [4][23][24][25], the Coulomb friction coefficient is usually chosen in the range between 0.2 and 0.3 for quasi-static analyses. In the current study, the frictional coefficient was initially set to 0.2 for contact between the profile and the rigid plates, while the self-contact between profile walls was initially set to 0.5. The friction coefficient is difficult to determine accurately, and a sensitivity study was conducted to

investigate the influence it has on the results. Even though some of the tests experienced minor cracking in the corners, it was decided to omit failure modelling in this study. This was mainly done because NaMo does not provide enough information to calibrate a failure criterion.

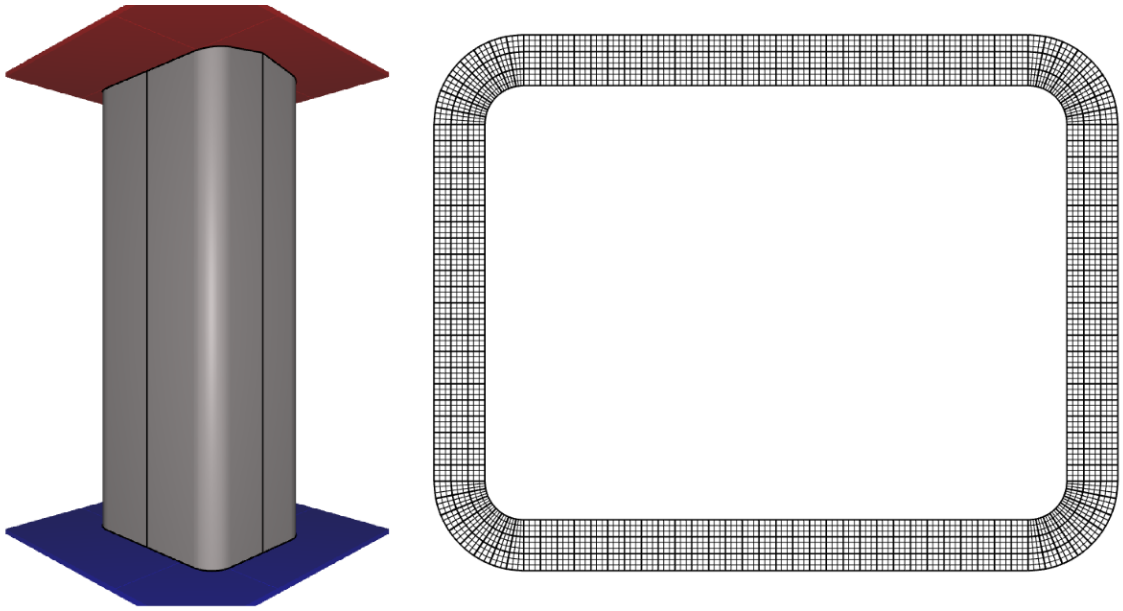

Figure 10: (a) FE model of the profile, the top plate and the bottom plate, (b) through thickness mesh of FE model.

4.2 Numerical results

Figure 11 shows the effect friction between the rigid parts and the profile has on the force-displacement curve for AA6061-T6 where the flow stress curve from NaMo was employed. It is evident that altering the friction coefficient slightly modifies the force-displacement curve. Especially around 20 mm displacement, a low friction coefficient results in a peak more prominent than in the experiments. A higher friction coefficient recreates this part of the force-displacement curve better. However, the last peak is better reproduced with a low friction coefficient. By inspection of the curves it is seen that all the tested friction coefficients provide acceptable results, and the recommendation of setting the coefficient in the range of 0.2 to 0.3 seems reasonable. Altering the friction coefficient for the self-contact between the profile walls showed negligible effect on the resulting force-displacement curve. Based on the results from the sensitivity study and recommendations from earlier studies, the friction coefficient between the rigid parts was changed to 0.3, while keeping the initial coefficient of 0.5 for the self-contact between profile walls for the rest of the study.

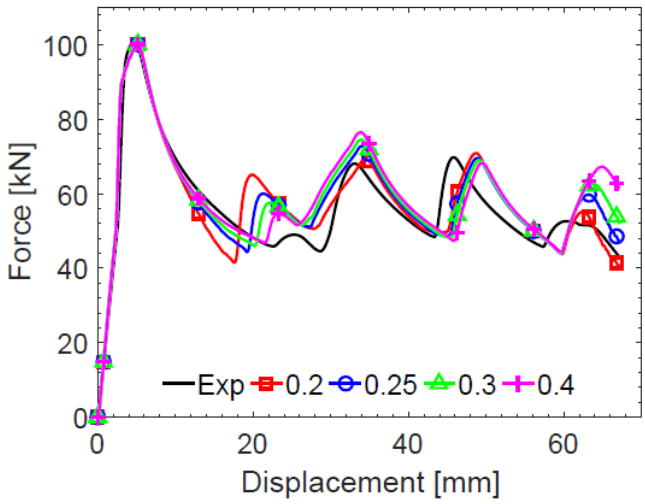

Figure 11: Force-displacement curves for the different friction coefficients between rigid parts and profile for AA6061-T6.

Figure 12 to Figure 14 compare the force-displacement curves from all the experiments and simulations, where the flow stress curve was based on either NaMo calculations or tensile tests. The shapes of the simulated force-displacement curves from both approaches are in good correspondence with the experimental curves, and it is evident that the FE model captures the overall behaviour. In five of the cases, the results from the two simulations are better matched to each other than with the experimental data. Somewhat surprisingly, the simulations with the flow stress curve based on tensile tests only comply better with the experimental data for two of the nine alloy-temper combinations. The simulations with the flow stress curve based on NaMo calculations give better agreement with the experimental results for two of the alloy-temper combinations. As the force-displacement curves from the crush test in Figure 4 displayed similar curves for AA6061-T7 and AA6110-T7, while the flow stress curves calculated by NaMo predicted a clear difference between these two alloy-temper combinations, it was expected that one of these simulations would be less accurate. Of the two simulations based on NaMo that are less accurate, one is overestimating the force level while the other one is underestimating it. Both sets of simulations predict the correct number of force peaks with the peaks occurring at approximately the same displacements as in the experiments.

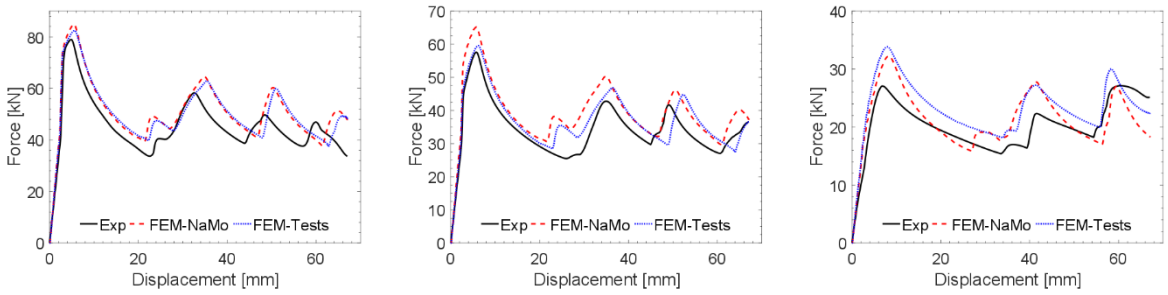

(a) AA6063-T6 (b) AA6063-T7 (c) AA6063-O

Figure 12: Force-displacement curves from experiments and FE simulations for AA6063.

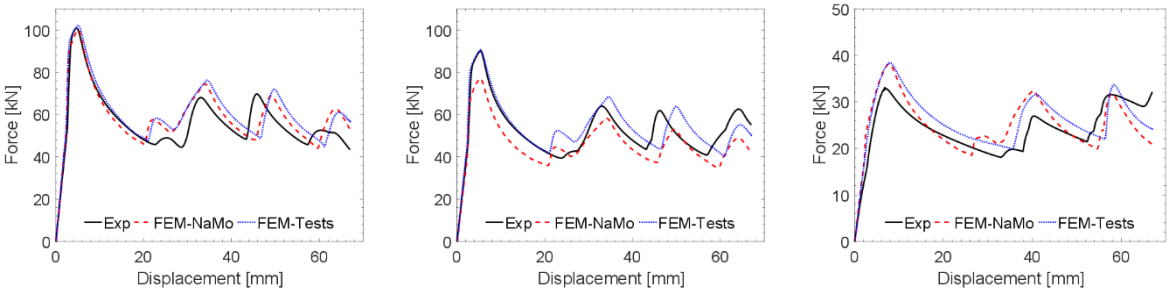

(a) AA6061-T6 (b) AA6061-T7 (c) AA6061-O

Figure 13: Force-displacement curves from experiments and FE simulations for AA6061.

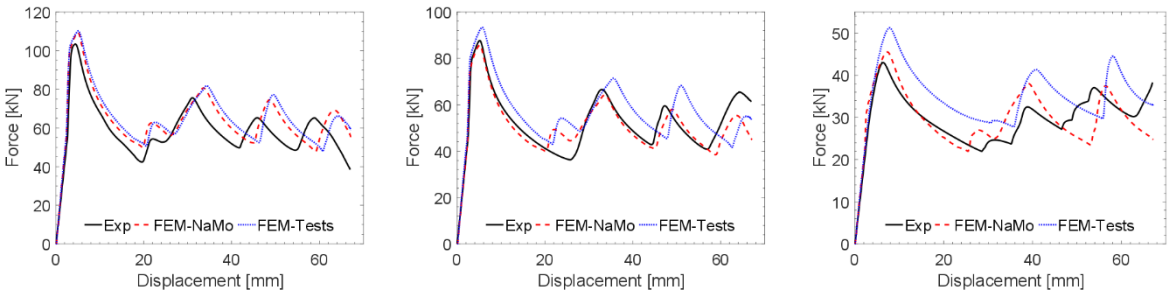

(a) AA6110-T6 (b) AA6110-T7 (c) AA6110-O

Figure 14: Force-displacement curves from experiments and FE simulations for AA6110.

The peak and mean forces from the experiments and simulations are plotted against each other in Figure 15. The simulations with flow stress curve based on tensile tests yield consistent results, i.e., the simulated peak and mean forces are consistently somewhat higher than the experimental ones. Also the simulations based on NaMo data overestimate the peak and mean forces in most cases, except for AA6061-T7 and AA6110-T7 where the predicted forces are somewhat lower than the experimental ones. However, there is a distinct correlation between the accuracy in the simulated mean and peak forces for the two approaches. In the simulations based on NaMo data, the largest difference in peak force is 19 %, 14 % and 8 % for O, T7 and T6 temper, respectively, and the MAPE of the peak force is below 10 %. With flow stress curve based on tensile tests, the largest difference in peak force is 6 % for both T6 and T7 temper and 25 % for O temper, while the MAPE is again below 10 %. This is best visualized in Figure 12 to Figure 14. The largest difference in mean force is about 16 % for AA6063-T7 in the simulations based on NaMo data, while four alloy-temper combinations have a difference less than 5 % and the MAPE of the mean force is less than 8 %. The corresponding results for simulations based on tensile tests is about 18 % as the largest difference, while only one alloy-temper combination has a difference less than 5 % and the MAPE of the mean force is 10 %. In summary, the overall accuracy is equally good for the NaMo-based simulations as for those based on tensile tests.

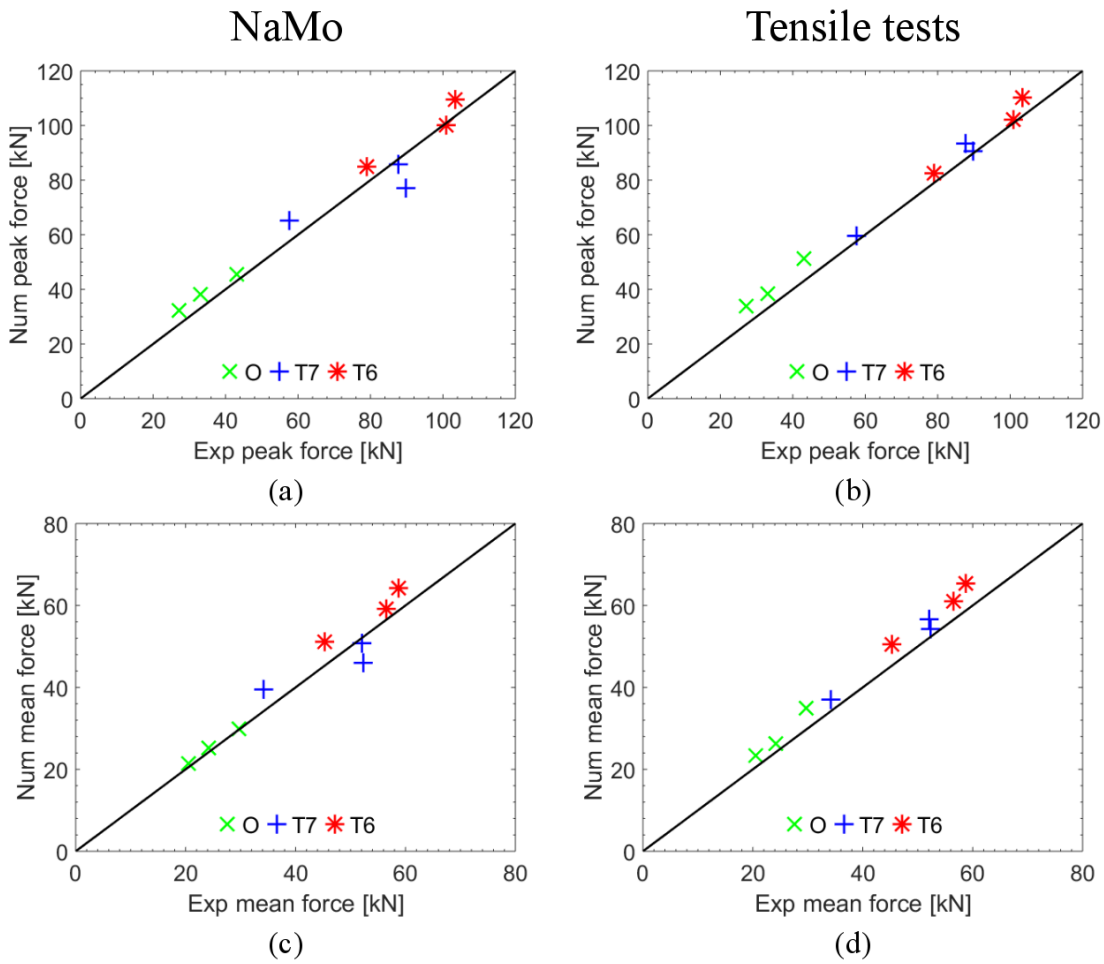

Figure 15: Scatter plots of (a) peak force from experiments and simulations using NaMo data and (b) with simulations using data from tensile tests. Scatter plots of (c) mean force from experiments and simulations using NaMo data and (d) with simulations using data from tensile tests.

5 Discussion

In Figure 16, the deformed RHS profile of an AA6061-T6 experiment is compared to the corresponding deformed FE mesh from a simulation based on NaMo data at given displacements. In total, five evenly spaced displacements are chosen, including the first and last frame. A plot marking these points on the force-displacement curve is given in Figure 17. The simulation is seen to capture the correct folding mode throughout the deformation and the conformity with the experiment is deemed excellent from this viewpoint. At a displacement $d = 16.75$ mm, the initiation of the first fold is recreated and developed correctly into the second fold at $d = 33.5$ mm. This is in accordance with the good conformity in the force-displacement curves up to this point. However, by inspection of Figure 16 and Figure 17 at a displacement $d = 50.25$ mm, it is evident that the simulation is diverging slightly from the experiment. The third fold is just commenced in the simulation, while in the experiment the third fold is already collapsing. This delayed response is seen to initiate during the development of the

second peak, where the difference in force magnitude allegedly contributes to this. The difference is assumed related to the work hardening as the aforementioned sensitivity study on the friction coefficient shows that friction has marginal influence on delaying the folding pattern. Despite the discrepancies in the force-displacement curve at the final deformation, the agreement is qualitatively good. In the bottom fold in the experiment, a crack is seen in the corner, which is not present in the simulation since a failure criterion is omitted. However, the incipient fracture is seen to have negligible influence on the global response, coinciding with the findings in Ref. [26].

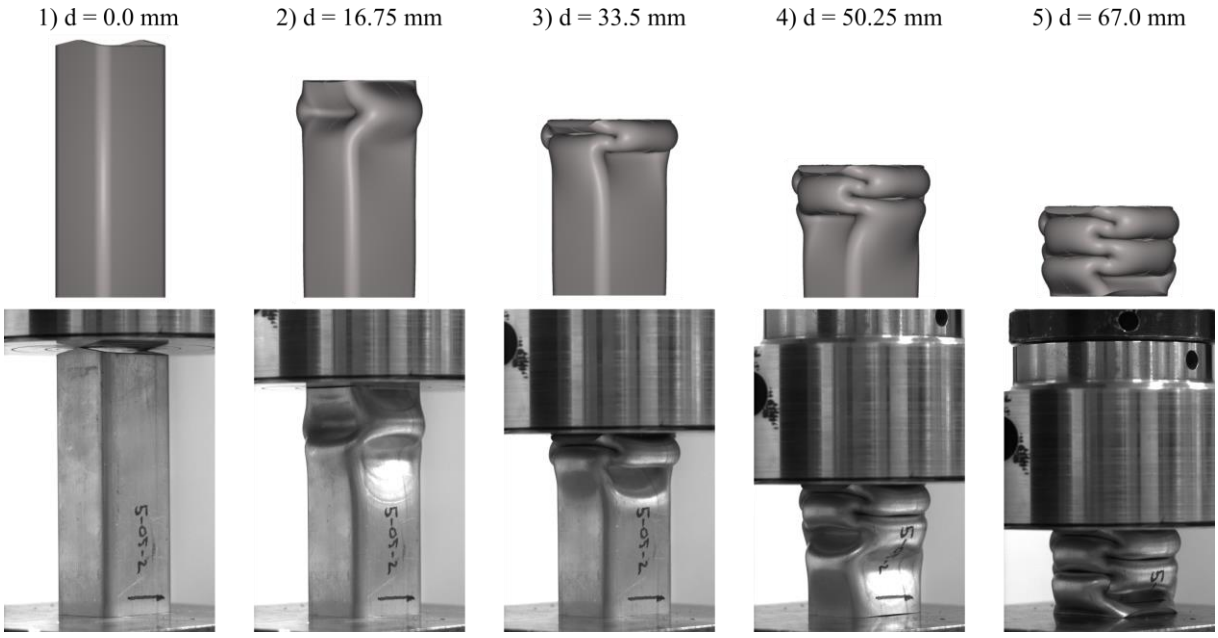

Figure 16: Comparison of deformation patterns in experiment and simulation with NaMo data of AA6061-T6.

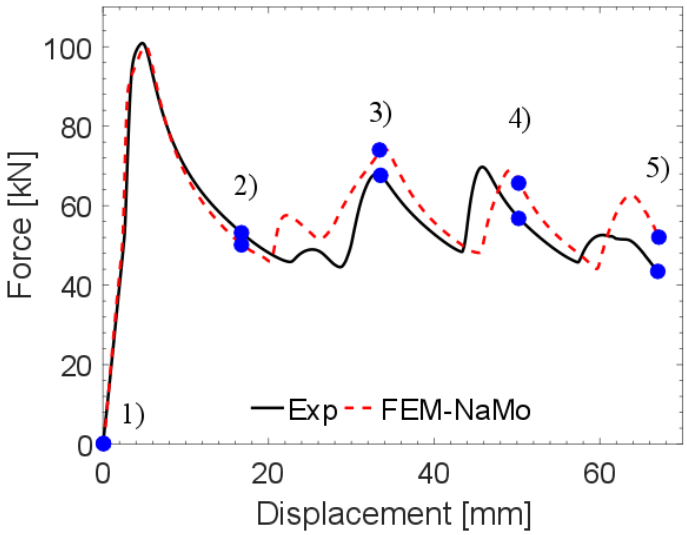

Figure 17: Comparison of force-displacement curves between experiment and simulation with NaMo data of AA6061-T6 where the markers conform with the displacements in Figure 16.

Among the uncertainties introduced in the FE model, friction between the rigid parts and the profile is an important one which is difficult to determine. Figure 16 showed an excellent agreement between experiment and simulation with respect to the folding pattern seen from the side. In Figure 18, the bottom of the deformed profiles is seen from below, showing a comparison between the experimental and numerical results obtained with NaMo data. The shapes vary considerably from the T6 temper to the O temper, and even though one could argue that the trends are captured by the numerical model, discrepancies are seen, especially for the O temper. In the simulations of the O temper, the profiles are collapsing more than what is observed in the corresponding experiments. By visual inspection of the folding process, one can see that the bottom of the profile remains rectangular until approximately the last 10 mm of deformation. It is presumed that the discrepancies in this part of the force-displacement curves are reflected in the discrepancies in the deformation patterns of the bottom part of the profile. Discrepancies are also seen for AA6063-T6 and AA6110-T6 where the profile is seen to collapse more in the experiment than in the simulation. It is expected that the discrepancy in the folding pattern of the profiles is a result of the combined effects from inaccurate description of the friction between the rigid parts and the profile, and the predicted flow stress by NaMo. However, simulations based on the tensile tests did not give particularly better results for this problem. Based on the quantitative comparisons between the experiments and the simulations it is hard to imagine that there exists a constant friction coefficient reproducing the bottom shape of all the nine alloy-temper combinations correctly.

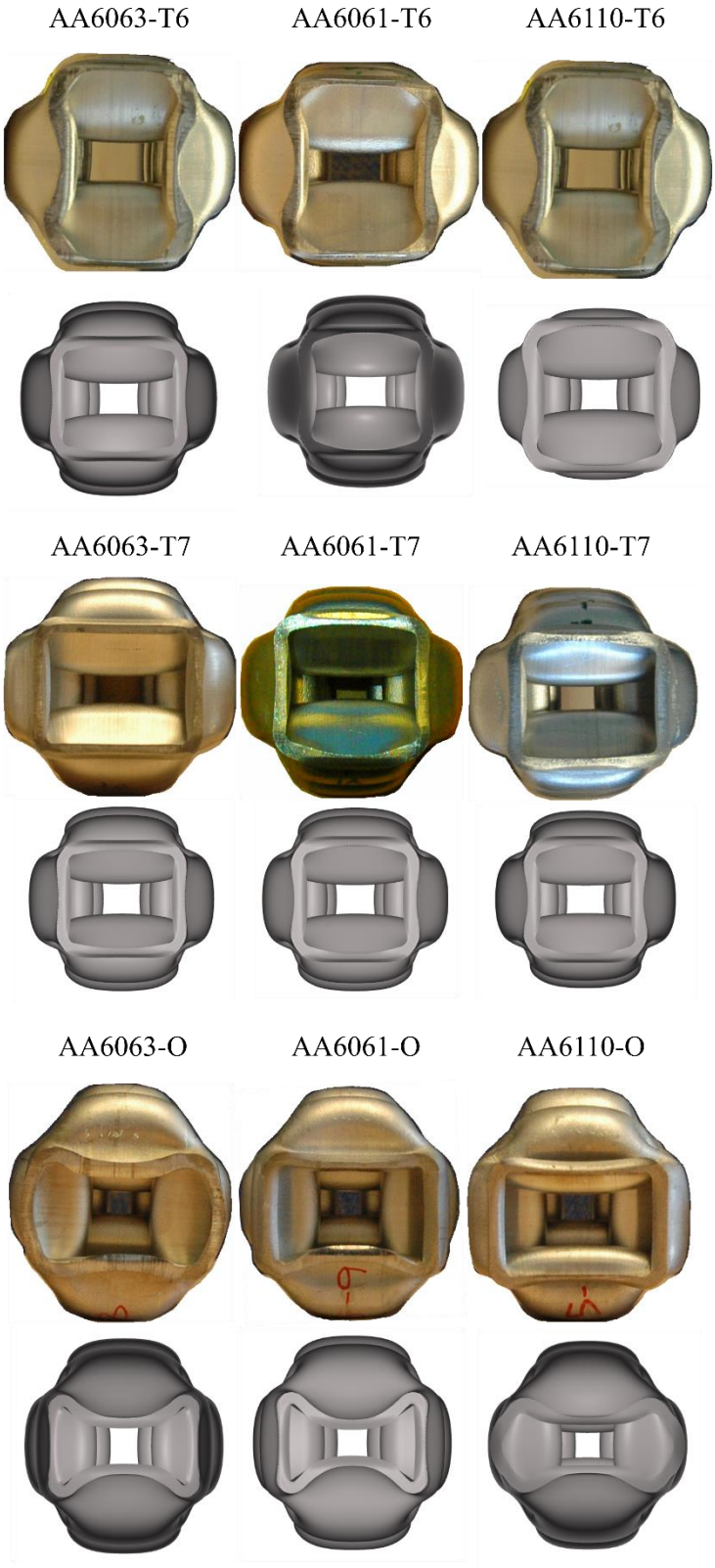

Figure 18: Comparison of the deformation patterns of the bottom part of the profiles in experiments and simulations (based on NaMo data) as seen from below.

It should be pointed out that the almost perfect match between the experimental and numerical results with NaMo data for some alloy-temper combinations may be somewhat coincidental, keeping

in mind that a number of assumptions have been made in the entirely numerically obtained results. In addition, the fact that the simulation of the RHS profile introduces a number of interfering factors may contribute to balance out potential errors caused by NaMo. Especially in the mean force calculations, some discrepancies are seen to neutralize each other and thus give better results than expected. However, when considering the crushing of the RHS profiles, the results provided by the use of NaMo are as accurate as those obtained based on tensile tests, suggesting that other factors than the accuracy of the flow stress curve are as crucial for the actual problem. One can justify the use of NaMo for this application provided that the energy absorption and folding process are of main interest and that failure plays an insignificant role.

6 Concluding remarks

In this paper, nanostructure-based FE simulations of quasi-static axial crushing of rectangular hollow section profiles made of AA6063, AA6061 and AA6110 in tempers T6, T7 and O have been evaluated. The nanostructure model NaMo was employed to obtain the flow stress curves, where the chemical composition and thermo-mechanical history are used as input. The flow stress curves were then transferred to the IMPETUS Afea Solver used to simulate the quasi-static axial crushing tests. A refined finite element model was employed to reduce discretization errors and enable validation of the NaMo simulations. To evaluate NaMo for the actual application, tensile tests were conducted to obtain calibrated flow stress curves and these were employed in additional simulations of the quasi-static axial crushing tests. For validation purposes, an experimental program on crushing of RHS profiles was conducted with two repetitions of each alloy-temper combination, resulting in 27 tests. The parallel tests demonstrated excellent repeatability, which was substantiated by the conformity in the force-displacement curves.

When comparing the numerical results obtained with NaMo data to the experimental results, provided as force-displacement curves, peak and mean force scatter plots, an excellent overall agreement was found, taking into consideration that no experimental data were used to calibrate the material model. Excellent agreement was also found by visual inspection of the deformation of the profiles. However, some discrepancies were observed when inspecting the bottom part of the profiles seen from below, indicating among others that friction between the rigid parts and the profile may not be correctly described for all alloy-temper combinations by a constant friction coefficient. The performance of the FE model was deemed good as the number and magnitude of peaks in the force-displacement curves were adequately predicted, combined with the excellent correspondence in the

deformation process. The simulations with flow stress curves based on tensile test data exhibited about the same level of accuracy as those based on NaMo data. The MAPE of the peak force was about 10 % for the two sets of simulations, while the MAPE of the mean force was around 8 % and 10 % for the simulations based on NaMo data and tensile test data, respectively.

The performance of the nanostructure model NaMo has been assessed in this study. The results show that we can predict quasi-static axial crushing of RHS profiles made of AA6xxx aluminium alloys with good accuracy, without carrying out a single material test. The robustness of the model is verified by employing materials with different chemical composition and thermo-mechanical history. The capability of the model to predict the material behaviour of an alloy based on its chemical composition and the thermo-mechanical history, makes it useful for developing tailored alloys and reducing the need for expensive and time-consuming test programs in design of aluminium structures made of 6xxx alloys.

Acknowledgment

The authors gratefully appreciate the financial support from NTNU and the Research Council of Norway through the FRINATEK Programme, Project No. 250553 (FractAl). The authors would like to thank Mr. Trond Auestad for managing the experimental tests and Mr. Eivind Sogn Kjus and Mr. Espen Solhjem for their contribution in the experimental work. The authors would also like to thank Dr. Ulf Tundal from Hydro Aluminium, Mr. Martin Lefstad and Mr. Arne Gellein from SINTEF Materials and Chemistry for their contribution with the extrusion of the profiles. Lastly, the authors would like to thank Ms. Helen Langeng from SINTEF for conducting the artificial ageing of the profiles.

References

[1] O.R. Myhr, O. Grong, K.O. Pedersen, A combined precipitation, yield strength, and work hardening model for Al-Mg-Si alloys, Metallurgical and Materials Transactions A: Physical Metallurgy and Materials Science 41 (9) (2010) 2276–2289.

[2] J. Johnsen, J.K. Holmen, O.R. Myhr, O.S. Hopperstad, T. Børvik, A nano-scale material model applied in finite element analysis of aluminium plates under impact loading, Computational Materials Science 79 (2013) 724–735.

[3] J.K. Holmen, T. Børvik, O.R. Myhr, H.G. Fjær, O.S. Hopperstad, Perforation of welded aluminum components: Microstructure-based modeling and experimental validation, International Journal of Impact Engineering 84 (2015) 96–107.

[4] N.H. Hoang, O.S. Hopperstad, O.R. Myhr, C. Marioara, M. Langseth, An improved nano-scale material model applied in axial-crushing analyses of square hollow section aluminium profiles, Thin- Walled Structures 92 (2015) 93–103.

[5] O. Engler, C. Schäfer, O.R. Myhr, Effect of natural ageing and pre-straining on strength and anisotropy in aluminium alloy AA 6016, Materials Science and Engineering A 639 (2015) 65–74.

[6] X. Zhang, G. Cheng, H. Zhang, Theoretical prediction and numerical simulation of multi-cell square thin-walled structures, Thin-Walled Structures 44 (11) (2006) 1185–1191.

[7] X. Zhang, Z. Wen, H. Zhang, Axial crushing and optimal design of square tubes with graded thickness, Thin-Walled Structures 84 (2014) 263–274.

[8] H. Sun, J. Wang, G. Shen, P. Hu, Energy absorption of aluminum alloy thin-walled tubes under axial impact, Journal of Mechanical Science and Technology 30 (7) (2016) 3105–3111.

[9] A. Hanssen, M. Langseth, O.S. Hopperstad, Static and dynamic crushing of circular aluminium extrusions with aluminium foam filler, International Journal of Impact Engineering 24 (5) (2000) 475–507.

[10] T. Børvik, O.S. Hopperstad, A. Reyes, M. Langseth, G. Solomos, T. Dyngeland T, Empty and foam-filled circular aluminium tubes subjected to axial and oblique quasi-static loading, International Journal of Crashworthiness 8 (5) (2003) 481–494.

[11] X. Zhang, G. Cheng, A comparative study of energy absorption characteristics of foam-filled and multi-cell square columns, International Journal of Impact Engineering 34 (11) (2007) 1739–1752.

[12] M. Langseth, O.S. Hopperstad, A. Hanssen, Crash behaviour of thin-walled aluminium members, Thin-Walled Structures 32 (1-3) (1998) 127–150.

[13] H. Zarei, M. Kröger, Crashworthiness optimization of empty and filled aluminium crash boxes, International Journal of Crashworthiness 12 (3) (2007) 255 – 264.

[14] M. Costas, D. Morin, M. Langseth, L. Romera, J. Díaz, Axial crushing of aluminum extrusions filled with PET foam and GFRP. An experimental investigation, Thin-Walled Structures 99 (2016) 45–57.

[15] M. Costas, D. Morin, M. Langseth, J. Díaz, L. Romera, Static crushing of aluminium tubes filled with PET foam and a GFRP skeleton. Numerical modelling and multiobjective optimization, International Journal of Mechanical Sciences 131-132 (2017) 205–217.

[16] IMPETUS Afea AS, IMPETUS Afea Solver, http://www.impetus-afea.com/ [cited 16/08-2017].

[17] T. Tryland, T. Berstad, Keep the material model simple with input from elements that predict the correct deformation mode, 10th European LS-DYNA Conference 2015, Würzburg, Germany

[18] A.V. Hershey, The plasticity of an isotropic aggregate of anisotropic face centered cubic crystals, Journal of Applied Mechanics, 21 (3) (1954) 241 – 249.

[19] F. Barlat, H. Aretz, J.W. Yoon, M.E. Karabin, J.C. Brem, R.E. Dick, Linear transformation-based anisotropic yield functions, International Journal of Plasticity, 21(5) (2005) 1009 – 1039.

[20] O.R. Myhr, O. Grong, C. Schäfer, An Extended Age-Hardening Model for Al-Mg-Si Alloys Incorporating the Room-Temperature Storage and Cold Deformation Process Stages, Metallurgical and Materials Transactions A: Physical Metallurgy and Materials Science 46 (12) (2015) 6018–6039.

[21] M.F. Ashby, The deformation of plastically non-homogeneous materials, The Philosophical Magazine, 21 (8) (1970) 399 – 424.

[22] J.K. Holmen, J. Johnsen, O.S. Hopperstad, T. Børvik, Influence of fragmentation on the capacity of aluminum alloy plates subjected to ballistic impact, European Journal of Mechanics, A/Solids 55 (2016) 221–233.

[23] X.W. Zhang, H. Su, T.X. Yu, Energy absorption of an axially crushed square tube with a buckling initiator, International Journal of Impact Engineering 36 (3) (2009) 402–417.

[24] M. Langseth, O.S. Hopperstad, T. Berstad, Crashworthiness of aluminium extrusions: validation of numerical simulation, effect of mass ratio and impact velocity, International Journal of Impact Engineering22 (9-10) (1999) 829–854.

[25] D. Karagiozova, G.N. Nurick, S. Chung Kim Yuen, Energy absorption of aluminium alloy circular and square tubes under an axial explosive load, Thin-Walled Structures 43 (6) (2005) 956–982.

[26] M. Langseth, O.S. Hopperstad, Static and dynamic axial crushing of square thin-walled aluminium extrusions, International Journal of Impact Engineering 18 (96) (1996) 949–968.